Acta Materialia 237 (2022) 118148

Contents lists available at ScienceDirect

Acta Materialia

journal homepage: www.elsevier.com/locate/actamat

Full length article

Microstructural evolution of lamellar Fe-25Ni foams during steam-hydrogen redox cycling

Jacob B. Mack[1,*], Samuel M. Pennell[1], David C. Dunand

Department of Materials Science and Engineering, McCormick School of Engineering, Northwestern University, 2220 Campus Drive, Evanston, IL 60208, USA

ARTICLE INFO

Article history:
Received 11 April 2022
Revised 1 July 2022
Accepted 2 July 2022
Available online 4 July 2022

Keywords:
Metal-foam
X-ray diffraction
Alloys
Microstructure
Oxidation

ABSTRACT

Cyclical steam oxidation and hydrogen reduction, relevant to iron-air batteries, is performed on freeze-cast Fe-25Ni (at.%) foams consisting of colonies of parallel lamellae separated by channels, both ~20 μm thick and millimeters in length. This structure is designed to accommodate volumetric changes associated with the cyclical oxidation and reduction of Fe. Metallographic imaging performed at various redox stages, together with time-resolved *in situ* X-ray diffraction during redox cycling, detail the reaction kinetics and phase evolution of the foam, the evolution of its lamellar microstructure, and the eventual degradation of its internal architecture. As Fe preferentially oxidizes over Ni, each lamella develops an outer Fe-oxide scale, with metallic Ni rejected to the cores of the lamellae which develops an interconnected network of Fe-oxide veins. The Ni-rich metallic core limits the accumulation of Kirkendall pores and provides adhesion to the Fe-oxide scale, thus preventing lamellar fracture observed in unalloyed Fe foams. While the oxidation rate is slowed by the presence of Ni, the reduction rate is accelerated, as Ni acts as a catalyst and as the network of oxidized veins reduces quickly and become open microchannels, thereby providing rapid hydrogen access (driving reduction) and steam egress to the lamellar interior. After complete reduction, the Fe-rich shell and the Ni-rich core interdiffuse and homogenize, which helps eliminate both Kirkendall pores and microchannels from the lamellae. Furthermore, the ductile Ni-rich core limits lamellar buckling (another densification mechanism active in Fe foams). Architectural changes also affect resistance to internal damage, with smaller lamellar colonies exhibiting better resistance to buckling. These combined effects provided by Ni alloying allow the Fe-25Ni foams to maintain a high channel porosity (>40% porous), and thus high active surface area, after 10 redox cycles, as compared to a near complete loss of open channel porosity reported in unalloyed Fe foams.

1. Introduction

Iron-air batteries stand out as an environmentally-sustainable, inexpensive and thus scalable alternative to Li-ion batteries and other commercial technologies for large-scale grid electrochemical storage [1–6]. In operation, the redox-active Fe material acts as an energy storage system in tandem with a reversible solid oxide fuel cell which performs as a charger/discharger. During discharge, metallic iron is oxidized to iron oxide with steam, thus producing hydrogen which is then combined with oxygen from air at the anode of the fuel cell, creating an electrical current; during charging, the reaction is reversed, with iron oxide being reduced to metallic iron with hydrogen produced by the fuel cell, releasing steam [7–9]. For this reversible Fe/Fe-oxide reaction to take place at sufficiently high rates, the battery must be operated at elevated temperatures (500-800°C), similar to those of the oxide fuel cell whose waste heat can thus be used.

The volumetric expansion on oxidation (up to 110% for the Fe → Fe_3O_4 reaction) and the subsequent contraction on reduction drive densification and sintering in Fe powder-bed redox systems, drastically shortening the lifetime of the Fe-air battery [10–12], in a mechanism reminiscent to (de)lithiation cycling damage in Si-based batteries [13–15]. In our previous work, lamellar Fe foams were fabricated with sufficient channel porosity to accommodate these large volumetric changes [16–18], but rapid degradation was still observed during redox cycling. This stems from two main mechanisms: (i) formation of Kirkendall porosity within lamellae, due to imbalanced diffusion of Fe ions outward and O ions inward, leading to irreversible lamellar microporosity, (ii) fracture of the Fe lamellae due to mismatch stresses and brittleness of the oxide layer. These mechanisms induce widening and buckling of lamellae, which then contact neighboring lamellae and sinter

* Corresponding author.
E-mail address: jacobmack2022@u.northwestern.edu (J.B. Mack).
[1] These authors contributed equally to this work.

https://doi.org/10.1016/j.actamat.2022.118148
1359-6454/

together; this drives densification of the foam within the first few redox cycles. Densification is especially severe at the outer surface of the foam, where the contact and sintering between neighboring lamellar tips forms a dense shell that blocks gas access to the foam interior, slowing successive redox cycles.

To prevent these degradation mechanisms, we continue investigation into the effects of alloying Fe with Ni, which was previously shown to have a stabilizing effect during redox reactions [19], on the foam microstructure and bulk morphology [20]. Nickel is not oxidized by steam under the conditions used here and it thus acts as an inert metallic phase providing a range of benefits to the lamellar foam structure. First, metallic Ni within oxidized iron lamellae can decrease Kirkendall porosity by providing an additional interface for vacancy removal. Second, metallic Ni forms a ductile core within each lamella, and can provide mechanical stability to the otherwise brittle oxide layers that form during oxidation, thus preventing fracture during oxidation. Third, upon reduction, the Ni core adheres to the Fe-oxide scale on each lamella during volumetric shrinkage, thus helping prevent the degradation mechanisms listed above. As Ni forms a solid solution with Fe, the newly-reduced Fe coating on each lamella interdiffuses with the metallic Ni(Fe) core to reduce the concentration gradients; a full chemical re-homogenization to the original Fe-Ni composition can be achieved in the lamellae if sufficient time is allowed for interdiffusion after reduction. In this work, the Fe-25Ni (at%) composition was chosen to allow for a direct comparison to our previous work; this composition was found to have the best long-term redox cycling performance in previous investigations [20]. We detail the chemical and phase evolution of Fe-25Ni (at%) foams during redox cycling, we explore the role of submicron porosity on the microstructural evolution described previously [20], and we consider the long-term effects of these changes on the lamellar architecture with special consideration given to the additional effects of lamellar colony size.

2. Experimental procedures

2.1. Freeze casting

Fe-25Ni lamellar foams were fabricated using a water-based freeze-casting method, described in our previous work [16]. In short, an aqueous suspension was created by mixing α-Fe_2O_3 powder (Noah Technologies, 99.9%, $<$ 3 μm average), NiO nanopowder (Skyspring, 99.9%, 50 nm), and Zephrym PD 4974 dispersant (Croda, Inc.). The mass ratio of Fe_2O_3 and NiO powder was 3.21, corresponding to a Fe/Ni atomic ratio of 3, resulting in a Fe-25Ni (at%) alloy after reduction. The suspension, consisting of 10 vol% oxide powders and 0.5 vol% dispersant, was ball-milled for 48 h with zirconia balls (equal volume of media to slurry, 12 mm media) to eliminate agglomerates in the oxide powders. Polyethylene glycol binder (M_n=3350, Sigma Aldrich) dissolved in DI water was then added to the suspension for a total of 2 vol% binder in the suspension. Concentrated nitric acid was added dropwise to adjust the pH to the range of 5.5–6.5 which stabilizes the suspension, showing no tendency to settle during the casting and solidification procedures. The same procedure was used to fabricate pure Fe lamellar foams, with NiO omitted from the suspension.

Before freeze casting, the stabilized suspensions were degassed under mechanical vacuum, and then cooled to 1°C. A cylindrical Teflon mold (with height of 15 mm and inside and outside diameter of 15 and 25.4 mm, respectively) was placed on top of a Cu plate, and chilled to 1°C via a thermoelectric cooling device placed under the copper plate. Styrofoam insulation was placed around the mold to minimize radial temperature gradients. The chilled suspension was pipetted to fill the Teflon mold whose copper bottom was then cooled following an exponential profile, to achieve a constant freeze casting velocity of 16 μm/s for the suspension [21]. Once the Cu plate reached -30°C, the frozen sample with ~12–13 mm height and 15 mm diameter was punched out of the mold, and its bottom portion (~2 mm) was cut off to remove a thin sedimentation layer and provide a flat surface for freeze drying. The samples were then freeze-dried under vacuum (0.13 mbar) at -30°C for 48 h to sublimate the ice. The greenbody sample was then transferred to a tube furnace, where the binder was burned out at 300°C for 1 h under H_2 (Airgas, UHP). The foams were then reduced under H_2 at 600°C for 4 h, sintered under H_2 at 1000°C for 3.5 h, and cooled to room temperature, with a heating rate of 10°C/min and a cooling rate of 5°C/min throughout.

2.2. Redox cycling and characterization

To study redox conditions relevant to in an iron-air battery system, foams were cycled between alternative flows of H_2- and H_2O-rich gases at 800°C in a tube furnace. Initially, the temperature of each foam (8–9 mm diameter, 4–6 mm height) was raised to 800°C at 10°C/min under a 100 sccm flow of pure H_2. Then, a 60 min oxidation half-cycle was conducted under a 120 sccm flow of steam-saturated Ar, created by bubbling Ar (99.999% pure) through water at 93°C (to achieve a H_2O partial pressure of 0.77 atm). The subsequent 90 min reduction half-cycle used pure H_2 (200 sccm). After one or more such redox cycles, the foams were cooled at 10°C/min under flowing H_2 (100 sccm) when ending at the end of a reduction step. When ending during a step where the foam is partially oxidized, foams were instead cooled under Ar-4%H_2 (20 sccm) to minimize reaction during cooling. Foams were measured and weighted before and after cycling, and mass change was used to calculate extent of reaction between Fe and Fe_3O_4 (full conversion associated with a mass gain of ~25%) for the cycle times above. Foam volumes were calculated as a cylindrical volume, utilizing measured diameter and height.

Foams were vacuum-mounted in epoxy (Epothin 2, Buehler), ground to halfway through their height, and the resulting radial cross-sections were polished via standard metallographic procedures, with a final polishing step using a 1 μm diamond suspension. An optical metallography microscope (MA200, Nikon) was utilized to produce a macrograph of the entire cross section, assembled from stitching together 5x magnification images. In ImageJ, this was converted to a binary image displaying metallic lamellae and background (channels). These images were then processed by twice applying a median filter (radius of 1 pixels) to eliminate micropores from the calculated statistics. Interlamellar channel porosity was calculated by taking the ratio of lamella area to total sample area. The plug-in "Local Thickness" [22] was applied to the filtered image to calculate lamellar wall thickness, and (using an inverted image) channel thickness. Previous tomography studies have confirmed that these measurements on full 2D cross-sections are representative of the bulk foam [18,23].

Scanning electron microscope and energy-dispersive x-ray spectroscopy imaging were performed with the JEOL 7900F and the Hitachi 8030 electron microscope, under 15 kV accelerating voltage and 10 μm probe current, on mounted foams which had been sputter-coated with 10 nm of Au-Pd alloy prior to imaging. Samples investigated for the submicron channel network were additionally ion milled on a LEICA TIC3X to remove surface damage and increase resolution. Chemical analysis of foams was performed via combustion analysis (in accordance per ASTM E1019-18 (C)) by Westmoreland Mechanical Testing & Research (Youngstown, PA).

2.3. In-situ *X-ray diffraction*

In-situ XRD spectra were collected on a Stadi-MP (Stoe, Germany) instrument, with an asymmetric curved germanium

monochromator under pure Ag-$K_{\alpha 1}$ radiation ($\lambda = 0.5594$ Å) and a one-dimensional silicon strip-detector (MYTHEN2 1k, from Dectris, Switzerland), operated at 40 kV and 40 mA (Beam Size 4 × 0.8 mm). Data were collected in transmission in Debye-Scherrer geometry, using 12 s scans for 2θ angles between 10.7 and 29.2°, after calibration against a NIST Si standard (640d). A representative colony of lamellae was cut with a razor blade from a reduced and sintered Fe-25Ni foam, measuring 1–1.5 mm in height and ~0.5 mm in thickness, and introduced into a 1.5 mm diameter quartz capillary. Amorphous quartz wool was then packed into the capillary on either side of the sample, and the remaining volume of the capillary on both sides was filled with porous ceramic blocks to prevent sample movement during changes in gas flow. The loaded capillary was placed into a graphite-heated, water-cooled furnace, allowing for rapid heating and cooling, with a temperature stability of 0.1 °C. The foam was first heated to 800 °C at 30 °C/min under Ar-4% H_2 and held isothermally for redox cycling. For oxidation, Ar was bubbled (50 sccm) through 93 °C water, and the argon-steam gas mixture was then flowed into the capillary via copper tubing, heated to prevent steam condensation. For reduction, Ar-4% H_2 was flowed (50 sccm) through the capillary, using dilute hydrogen to slow the reduction kinetics.

Processing of diffraction spectra was done in Python and waterfall spectra plots were created using the Cmocean package [24]. To determine intensity and lattice parameter values, all spectra are first background-corrected using asymmetric least-squares smoothing [25]. Individual peaks are then fit using the lmfit package, modeling Pseudo-Voight profiles [26]. Integrated peak areas are calculated directly from the Pseudo-Voight fit. Peak centers are first converted to lattice parameter, and then converted to a relative change (expressed in %) in lattice parameter relative to the maximum lattice parameter observed for each compound throughout the experiment. To reduce noise in both peak area and lattice parameter data, binning is used; the scans were binned per six scans and the median value of the bin was taken as representative. The binned data were normalized to the highest median value. Both binned data and raw data are presented.

3. Results and discussion

3.1. Reaction kinetics and chemical evolution

To investigate the chemical and crystallographic changes associated with redox cycling of Fe and Fe-25Ni foams, *in-situ* XRD was performed to identify the phases present, the rate-limiting steps of the reaction, and the lattice parameters shifts due to compositional changes. An acquisition time of 12 s per diffraction spectrum was achieved by using a small sample with ~2% of the mass of a bulk foam, but containing numerous lamellae (Supplementary Fig. 1). To slow the high reaction rates associated with the small sample mass, a lower H_2 content (4%) was used in the reducing gas mixture, and slower gas flow rates were used for oxidation, as compared to bulk foams operating conditions. Due to these two modifications, the reaction times and kinetics derived from XRD experiments should not be directly compared to those derived from bulk foams; however, XRD results can be compared between the Fe and Fe-Ni foams.

3.1.1. Pure Fe foam

The redox process for a Fe foam is detailed in Fig. 1, which shows time-resolved diffraction peaks (Fig. 1a), and phase and lattice parameter changes with a max temporal resolution of 12 s, grouped into bins of 6 scans each; the median of each bin is plotted in the foreground with the raw data shown as a transparent overlay (Figs. 1b,c). Only part of the diffraction pattern is shown, highlighting the most intense reflections of the phases of interest: bcc-Fe (101), fcc-Fe(Ni) (111), FeO (111) (020), and Fe_3O_4 (131) (222) (400). The diffraction data are presented starting when the initial heating ramp to 800°C is completed. This heating ramp was conducted under flowing 4% H_2-Ar to ensure the sample did not oxidize before diffraction data were collected.

The foam is initially fully metallic, with a very small amount of FeO at t = 0 – 8 min (Fig 1a, orange arrow): since the furnace is heated under a reducing environment, this small FeO amount is likely formed due to trapped air in the gas lines prior to the experiment. At t = 10 min, showing the start of oxidation when the gas flow is switched to an oxidizing environment, this small FeO amount has been reduced. On the onset of oxidation, Fe is initially oxidized to wustite, the non-stoichiometric FeO phase. As oxidation proceeds (t = 10 – 25 min), this phase becomes richer in oxygen (expected to increase from ~51.3 to 52.7 at% O, based on the Fe-O phase diagram [27]), resulting in a lattice parameter decrease, visible as a shift of the peak center to higher diffraction angles. At t = 25 min, the wustite lattice parameter has decreased by ~ 0.7% from its original value. Locally, certain regions of the lamellae complete their Fe to FeO conversion and continue oxidizing to Fe_3O_4. These local differences in composition lead to the beginning of the FeO to Fe_3O_4 transformation (as early as t = 15 min) prior to the full disappearance of Fe (at t = 25 min), so that Fe, FeO and Fe_3O_4 co-exist in the foam for much of the oxidation period (t = 10 – 95 min). At t ~ 25 min, the metallic Fe phase has disappeared, as the FeO continues to transform to Fe_3O_4. The slight lattice parameter shift (about 0.2%) observed in the Fe phase is likely due to elastic strains in the remaining metallic portions, as the solubility of O in Fe at these temperatures is very low (0.002%) [27] and thus unlikely to cause this shift. As evident on the time-resolved data, this final FeO to Fe_3O_4 oxidation step to the equilibrium Fe_3O_4 takes significantly longer (80 min, from 15 to 95 min) than the initial conversion from Fe to FeO (15 min, from 10 to 25 min). During its formation, Fe_3O_4 does not display a lattice parameter shift, as expected from its stoichiometric composition (unlike FeO). Thus, at full oxidation of the Fe foam (t = 95 min), a complete conversion of Fe (iron) to Fe_3O_4 (magnetite) has occurred, consistent with the equilibrium phase expected between iron-oxide and steam [28].

At t = 95 min, H_2 reduction of the foam starts. Immediately, a small amount of Fe_2O_3 (hematite) is formed (green arrow, Fig 1a), resulting in decreased intensity of the Fe_3O_4 (magnetite) peak. While Fe_2O_3 is not expected to form under steam [28], residual air in the H_2 line provides an explanation for this transient Fe_2O_3 formation. As expected, Fe_2O_3 is quickly converted back to Fe_3O_4 as air is purged from the capillary, also explaining the 10 min delay in reduction from when the gas is switched (t = 105 min). Thereafter, the reduction pathway proceeds along the reverse path of oxidation; Fe_3O_4 is reduced to FeO, the FeO lattice parameter increases due to depletion of O, and finally, FeO is reduced back to metallic Fe. Once again, due to variations in local composition within different parts of the foam, these processes do not happen uniformly across the entire foam, resulting in the coexistence of Fe, FeO and Fe_3O_4 in the sample for some of the cycle. The Fe_3O_4 phase is fully reduced within 30 min, and most of the remaining FeO disappears in the next 10 min. However, at the end of the reduction half-cycle, after 75 min of reduction (t = 185 min), minor amounts of FeO remain present. This is likely due to entrapment of oxide, caused by fracture and then sintering of lamellae, limiting gas access to certain foam regions which shield the entrapped oxide (Supplementary Fig. 2). Additional Rietveld refinement was performed on the sum of the final five *in situ* scans (to increase signal to noise ratio) to resolve the phase fraction of entrapped oxide. This was found to be 7.2 wt% FeO, indicating 5% of the initial Fe was trapped as oxide after just 1 cycle. This illustrates a key degradation mechanism in

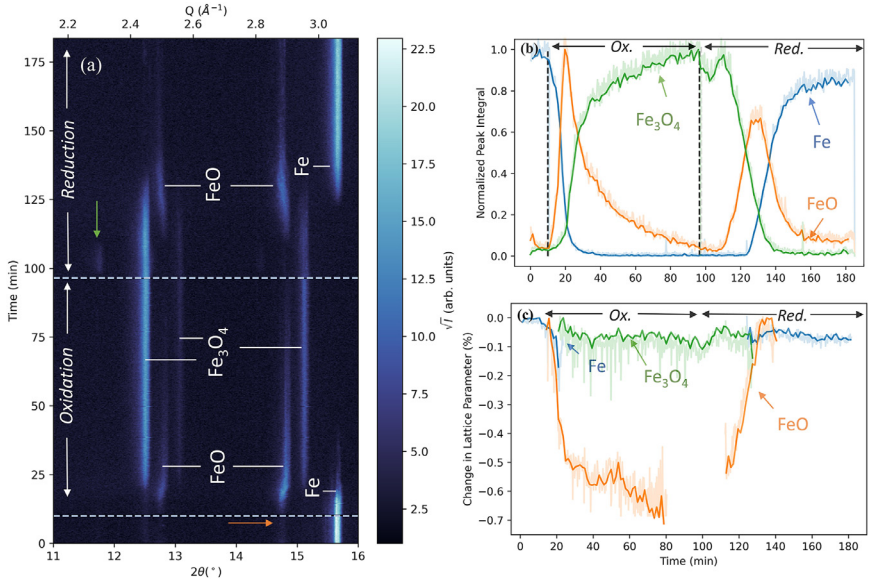

Fig. 1. *In-situ* XRD data of Fe foam during a first redox cycle. (a) Stacked XRD diffractograms as a function of time for the entire process. Intensity is scaled by taking its square root to reveal weaker oxide peaks. (b) Normalized intensity of each phase present throughout the process, measured from the most prominent peak of each phase (c) Lattice parameter changes for each phase, plotted only when a non-negligible amount of the phase is present. The following plane systems were used for peak intensity and lattice parameter: Fe <101>, FeO <200>, Fe_3O_4 <131>. For (b) and (c) the raw data, shown in transparent overlay, was binned into bins of six scans, the median of each bin was chosen as representative and all binned data were renormalized to reduce noise and remove outliers. "Ox" is short for oxidation, "Red" for reduction.

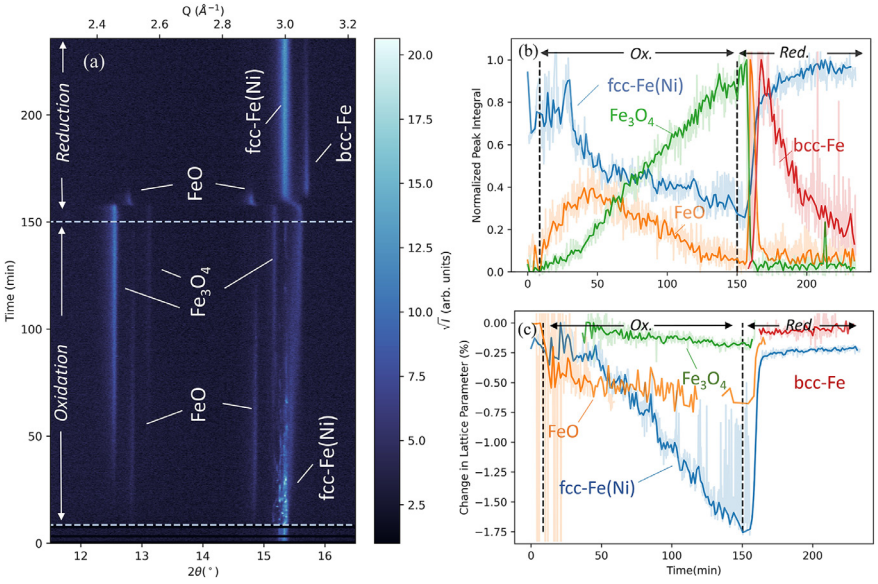

Fig. 2. *In-situ* XRD data of Fe-25Ni foam during a first redox cycle. (a) Stacked XRD diffractograms as a function of time for the entire process. Intensity is scaled by taking its square root to reveal weaker oxide peaks. (b) Normalized intensity of each phase present throughout the process, measured from the most prominent peak of each phase (c) Lattice parameter of each phase, tracked only when there is a non-negligible amount of the phase present. The following plane systems were used for peak intensity and lattice parameter: Fe-Ni <111>, Fe <101>, FeO <200>, Fe_3O_4 <131>. For (b) and (c) the raw data, shown in transparent overlay, were combined into bins of six scans, the median of each bin was chosen as representative and all binned data were renormalized to reduce noise and remove outliers.

the iron-air battery system, as remaining oxide after full reduction represents a loss of available capacity.

3.1.2. Fe-25Ni foams

The chemical evolution of an Fe-25Ni foam is shown in Fig. 2. The Fe-25Ni foam starts as an fcc-Fe(Ni) phase, as opposed to the pure bcc-Fe foam. Oxidation follows a similar path as that seen in the Fe foam (Fig. 1), with a first oxidation step to FeO followed by Fe_3O_4 formation. The Fe-25Ni foam shows an early and rapid shift in FeO lattice parameter; we hypothesize this indicates O-rich wüstite forms sooner as compared to the pure Fe foam. Despite the existence of ternary $NiFe_2O_4$ in the phase diagram (Supplementary Fig. 3), this oxide is not observed under our conditions, as confirmed by XRD. Further, the time evolution of oxide formation in Fe-25Ni is quite different than that for pure Fe. First, during oxidation, the fraction of FeO is always less than in the Fe foam, but FeO co-exists with Fe_3O_4 for longer times. The Fe_3O_4 phase fraction closely follows FeO, implying greater spatial inconsistency in local oxidation in the Fe-25Ni system than in pure Fe, leading to certain parts of the foam being oxidized to Fe_3O_4 while others are still undergoing Fe to FeO reactions. This is consistent with the microstructural evolution of Fe-based foams: for Fe to be oxidized,

it must first diffuse to the exterior edge of the Fe(Ni) compound, and then through any oxide layer present to the surface of the lamellae, where steam is present. In fcc Fe-25Ni, this diffusion is much slower than in bcc Fe [29]. This adds an additional, sluggish diffusion-controlled step in the Fe-Ni system, resulting in a longer oxidation period for these foams, lasting ~140 min (as compared to 90 min for Fe, Fig. 1(b)). The sluggish diffusion-controlled reaction becomes more evident as the reaction proceeds, with lower Fe content in the now Ni-rich lamellar core leading to a lower concentration gradient between the alloy core and the Fe-depleted scale interface. Because of this, as oxidation proceeds, the driving force for Fe diffusion to the surface declines, further slowing the reaction. Additionally, this provides a possible explanation for the early formation of O-rich wüstite.

The chemical evolution of the Ni-rich core of the lamellae is also visible in Fig. 2(a–c). Starting from Fe-25Ni (t = 0-10 min), an enrichment in Ni until t = 150 min is visible by a steady decrease in lattice parameter, up to a value of ~1.5%. The Fe-25Ni peak intensity also decreases, due to the removal of Fe by oxidation, and broadens, based on spatial variations in composition at the onset of oxidation. When the initial oxide scale has formed, relatively unchanged Fe-25Ni regions at the center of lamellae and Ni-rich shells at the scale interface coexist and have not yet homogenized. The lattice parameter for these two areas differ (2.9 Å for Fe-rich, 2.6 Å for Ni-rich), leading to the Fe(Ni) peak broadening at the start of oxidation. At full oxidation, only 88% of the initial Fe is fully converted to Fe_3O_4, as determined from mass change in bulk sample cycling, implying that some Fe remains in solid solution within the Ni-rich cores of the lamellae. This 88% conversion is consistent with the equilibrium composition in the computed Fe-Ni-O phase diagram (Supplementary Fig. 3). This represents a 12% loss in capacity with the addition of the Ni-core for this system as compared to the unalloyed Fe foam, beyond the loss due to the 25% Ni addition itself, as Ni does not partake in the redox reaction.

Upon reduction, Fig. 2 shows a lag of 7 min between the gas flow switch and the onset of reduction, again likely due to a slow flushing of steam present within the foam from the prior oxidation. No Fe_2O_3 is visible in the XRD pattern, unlike for the Fe foam. After this initial lag, reduction proceeds rapidly, with the Fe_3O_4 to FeO reduction completed in 2.5 min, and FeO to Fe in 6.5 min. The entire Fe_3O_4 to Fe reduction process thus occurs in ~ 9 min (as compared to 40 min for the Fe foam), illustrating the catalytic effect of Ni on iron oxide reduction, consistent with previous observations of Ni catalyzing reduction [30–32]. The acceleration of reduction kinetics at the metal-oxide interface occurs because newly formed oxygen vacancies can be removed at the interface at a much lower energetic cost than in the bulk material [33]. The FeO lattice parameter shift is consistent with that seen for pure Fe during reduction (Fig. 1c), as FeO becomes O-depleted before reducing to Fe.

During reduction, there is also a rapid lattice parameter shift for the fcc-Fe(Ni) phase, consistent with interdiffusion between the newly-reduced pure Fe at the surfaces of the lamellae and their Ni-rich Fe(Ni) cores (i.e., homogenization). The fast rate of this shift (occurring over 10 min) indicates the diffusion is dominated by surface diffusion as opposed to bulk diffusion. If only bulk diffusion were active the nominal diffusion distance for Fe-25Ni is less than 1 μm; since the lamellae, which has a half-width of 9 μm, is able to fully rehomogenize in 90 min, surface diffusion must be active [29]. After reduction, Ni-rich fcc-Fe(Ni) and Ni-poor bcc-Fe phases coexist, consistent with the shell of the lamellae being Fe-rich, as observed in the microstructural metallographic investigation to be discussed in a latter section. During the re-homogenization period, the intensity of the bcc-Fe peak decreases, as expected from homogenization, although a small amount of bcc-Fe still exists after 70 min of H_2 exposure. This signal most probably originates from Fe-rich regions which have lost diffusional contact with the fcc-Fe(Ni) core.

Overall, the addition of Ni in Fe foams significantly boosts the reduction rate, albeit at the cost of a slower oxidation rate, a lower specific capacity (as Ni does not oxidize) and higher material expenses (as Ni is more costly than Fe). Nevertheless, the lack of trapped oxide after the reduction steps (Fig. 2) represents a significant increase in reversibility of the anode material, potentially allowing for many more cycles of operation than a pure Fe foam.

3.2. Microstructure and architecture evolution

Understanding the compositional evolution of the foams informs our interpretation of their microstructural evolution; to confirm the results of the *in-situ* XRD tests in bulk samples and to observe the microstructural reversibility of the Fe-25Ni system, cycling was interrupted at various points during the first redox cycle on Fe-25Ni foams and the specimens were metallographically prepared and imaged. The foam's lamellar architecture is expected to help prevent the densification and loss of gas flow during redox cycling. The degradation mechanisms explored in pure-Fe foams [18] stem primarily from lamellar fracture due to internal stresses and the formation of Kirkendall porosity within the lamellae, leading to sintering and densification. Two strategies are possible, based on (i) avoidance of, and (ii) recovery from these microstructural changes during cycling. In our experiments, Fe and Fe-25Ni foams are cycled at 800°C, which is higher than normal operational temperatures for Fe-air batteries shown in recent work [3,7,34], and the redox cycling is performed to the full extent of the reactions. These high redox temperature and high degree of reaction likely exacerbate the degradation of the foams: our experiments can thus be considered an accelerated degradation study, relevant to lower-temperature operation under partial redox conditions.

3.2.1. Initial sintering of lamellar structure

After Fe-25Ni foam fabrication by oxide reduction, sintering and homogenization, the lamellae appear fully dense, showing little porosity in the radial cross section (Supplementary Fig. 4). Each lamella shows a homogeneous Ni concentration, as confirmed via EDS elemental maps (Supplementary Fig. 4), and as expected from the small interdiffusion distances provided by the oxide nanoparticles used during freeze-casting. Secondary dendrite arms are present (Supplementary Fig. 4, white arrows), as reported in similar freeze-cast structures studied previously [18]. The Fe and Fe-25Ni foams have low carbon content (<0.002 wt%), a common Fe contaminant, as confirmed by chemical analysis. Further, residual H_2 entrapment from the fabrication process is minimal (and thus has no significant effect on redox behavior): this was confirmed by adding a 20 h vacuum sintering step after foam fabrication, showing a lack of lamellar blistering that would be expected if gas micropores were entrapped within densified lamellae.

The microstructural evolution of the Fe-25Ni lamellae is strongly influenced by the presence of submicron porosity initially present within the lamellae; this porosity acts as a sink for Kirkendall pores, a barrier to diffusion, and a source for internal microchannels. Fig. 3 shows a schematic of the first redox cycle, with a focus on the submicron porosity. Each stage of this schematic is discussed in detail, along with experimental micrographs, in what follows.

A submicron porous network likely initially forms within each lamella during reduction and sintering of the foams, as H_2 reacts with the oxide micro- and nanoparticles (< 3 μm for Fe_3O_4 and

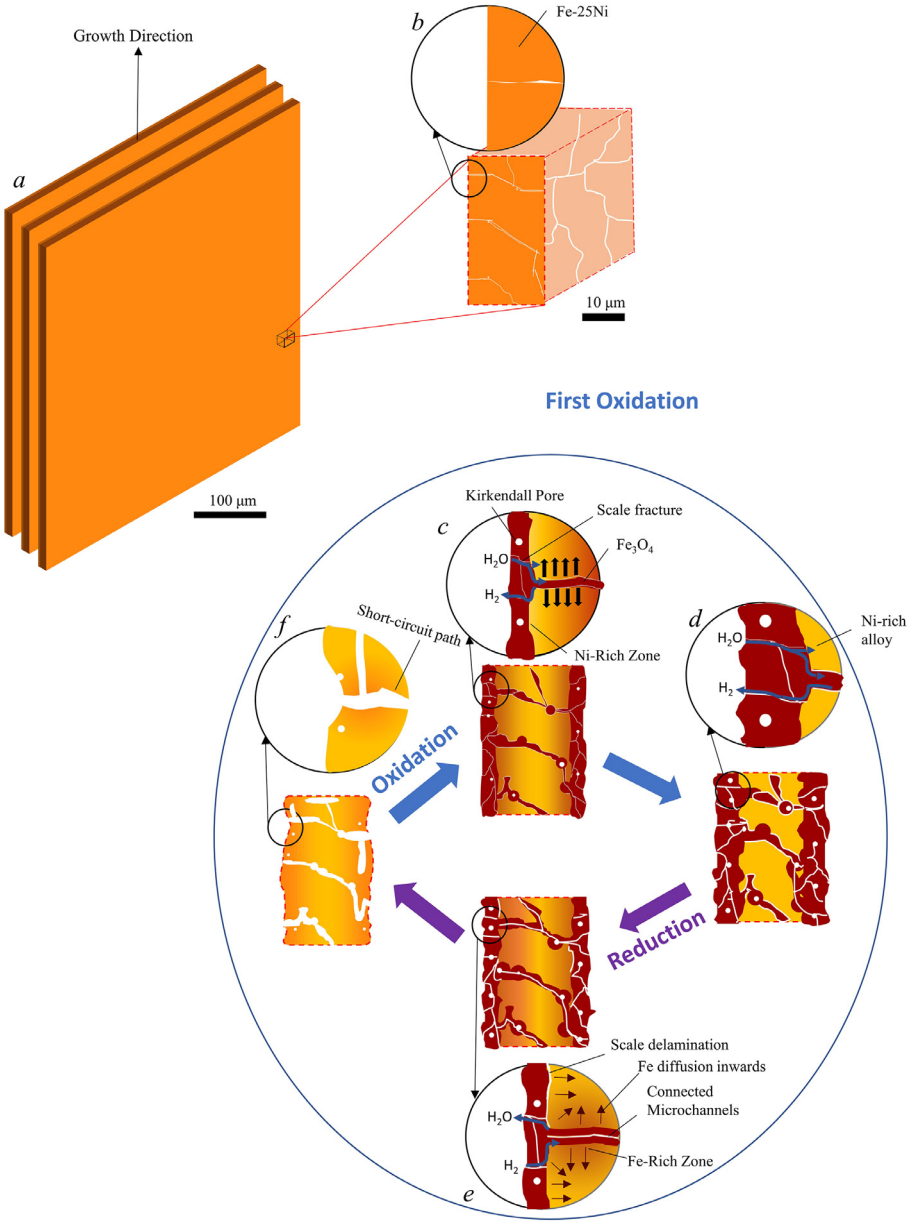

Fig. 3. Schematic illustrating the role of microchannels during microstructural evolution. Panel (a) shows a simplified 3-dimensional view of a lamellar series, with a sample volume indicated in black. A magnified view of this volume and its evolution are shown in the following panels: (b), a fully homogeneous, lamellar Fe-25Ni foam with submicron channels; (c) partially oxidized lamella, showing oxidation at surface and microchannels. The newly formed oxide scale develops Kirkendall micropores, and the diffusion of Fe to the oxidizing surfaces results in a gradient in Fe concentration from the core of the lamella to its outer surfaces; (d) fully oxidized lamella, with thick (~5 μm) scale forming a shell surrounding a Ni-rich core, intercrossed with oxide-filled microchannels. Kirkendall pores are prevalent in the scale (e) partially reduced lamella, with oxide reduction occurring at the interface between metal and oxide (both oxide scale and oxide microchannels). The volume contraction associated with Fe_3O_4 reduction cracks the oxide (containing previously formed Kirkendall pores) in the microchannels. Fe-rich areas close to the receding oxide scale are formed. (f) fully reduced lamella with partially homogenized Fe and Ni concentrations and interconnected microchannels as well as individual Kirkendall pores. Microchannels aligned with the direction of the concentration gradient allow for short-circuit diffusion, while microchannels oriented perpendicular to this gradient (formed due to scale delamination) slow diffusion by increasing the diffusion path length.

50 nm for NiO) to produce steam. This steam initially can escape through the particle interstices when the lamella has not fully sintered. However, as Fe- and Ni particles sinter and inter-diffuse to form a dense lamella, outflowing steam causes the formation of a submicron gas-egress network, observed after initial reduction and sintering via SEM imaging shown in Fig. 4.

These interconnected microchannels within each lamellae remain open to the lamellar surface while steam, created during oxide reduction by hydrogen, escapes; once reduction is complete, the microchannel network is difficult to close via further sintering because of the high aspect ratio and interconnectivity of the channels, unlike individual equiaxed pores which can sinter rapidly. While difficult to image due to their submicron diameters, these submicron channels can also be inferred from the lack of grain growth in the as-sintered structure shown in Fig. 4b, consistent with literature studies that show microporosity inhibits grain growth [35,36].

3.2.2. Oxidation

Fig. 5 shows optical micrographs, SEM micrographs, and corresponding EDS maps for 45%, 65%, and 100% oxidation of Fe. Oxidation initiates at the surface of the Fe-25Ni lamellae (Fig 5a,b), and

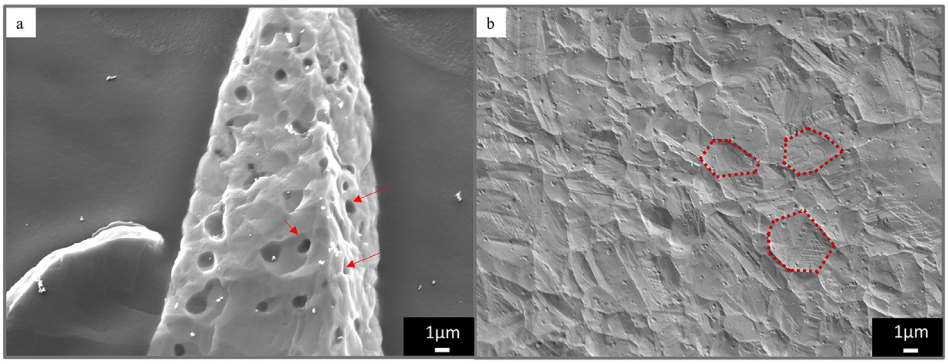

Fig. 4. SEM views of an Fe-25Ni lamella, in an as-fabricated foam after reduction and sintering (a) high-magnification cross-sectional view (ion milled) showing pores for steam egress / hydrogen ingress (black, three of which are highlighted with red arrows). (b) high-magnification side view of lamellar surface showing fine grain size, with red dashed lines outlining three grains visible on the surface of the lamella.

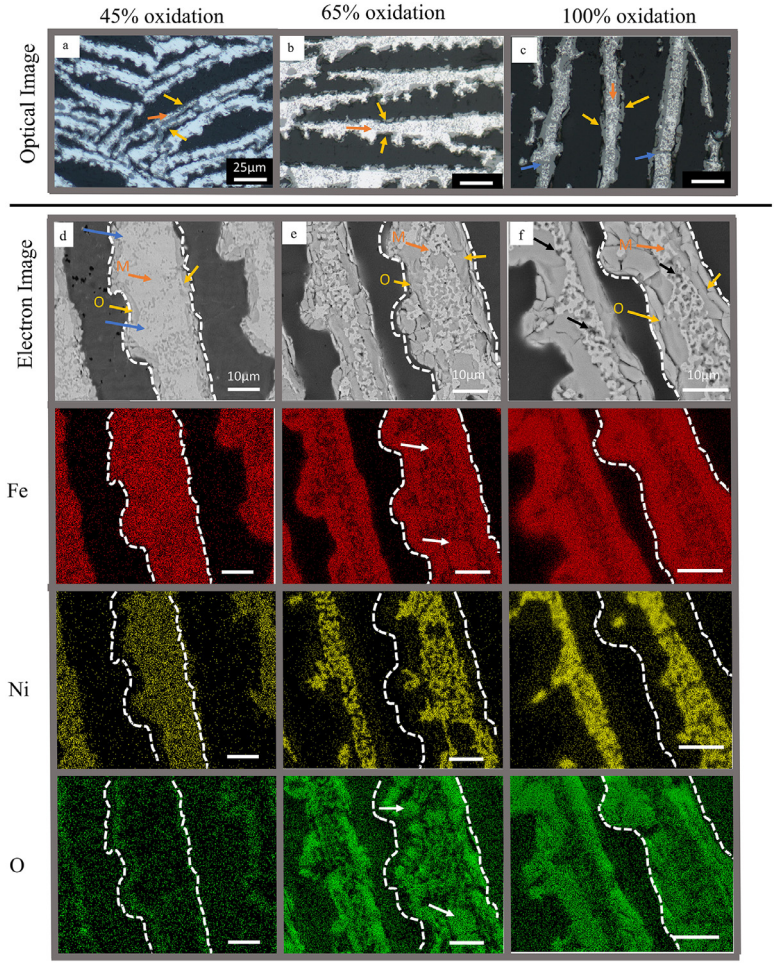

Fig. 5. Evolution of microstructure in Fe-25Ni lamellae during the first oxidation half-cycle, shown in radial cross sections with optical micrographs (a–c) and SEM micrographs with corresponding EDS maps (d–f) for 45% oxidation (10 min), 65% oxidation (15 min), and 100% oxidation (60 min). Yellow arrows indicate Fe-oxide scale (O) on lamellar surfaces. Blue arrows indicate oxide-filled microchannels. Orange arrows indicate metallic cores (M). Black arrows indicate coarsened Kirkendall pores. Dotted lines outline lamella surface to highlight differences in compositional makeup.

the oxide scale expands outwards due to the change of volume associated with oxide formation. The oxide growth is sustained by the outward diffusion of Fe-ions from the lamella metallic core through the oxide layer (via bulk diffusion), along with Ni rejection at the metal-oxide interface as Ni is not oxidized; the resulting compositional gradient within the metallic core leads to Ni inwards diffusion toward the lamella center, and Fe outward diffusion, as confirmed from compositional maps (Fig 5a).

Early in oxidation, oxide regions are visible within the interior of the lamella (Fig 5d, blue arrows), which appear partially connected to each other in the 2D cross-sections. These are not expected to be individual precipitates from internal oxidation as found for example in internally-oxidized Cu and Ag [37–39], since Fe oxidation proceeds from the surface, consistent with the small solubility of O in Fe. Rather, these regions are expected to be continuous veins of oxide connected in three dimensions to the

lamellar surface consistent with the internal porous network of microchannels (Fig. 3a, Fig 5a,b), which serves as an additional oxidation site within the volume of the lamellae. This network is expected to reduce the diffusion distance necessary for Fe atoms to diffuse to reach the reaction front. As they oxidize, the channels interconnectivity becomes more apparent, and they become part of the encroaching external scale layer to form a cohesive oxide frame that engulfs remaining Ni-rich regions (Fig. 5c), which are also expected to be connected in 3D.

Oxidation proceeds with the oxide scale growing in thickness on each of the lamellae (Fig 5c). The oxide scale thickness differs between lamellae at a given time (Fig 5c). This implies that the oxidation rate in various regions of the foam is not uniform, an expected result due to the tortuous path for gas flow through the foam and thus gradient in steam concentration near the foam surface and deeper in its interior. At the lamellar level, Fe concentration gradients becomes steeper as oxide forms in the microchannels within each lamella, located at the gas access points mentioned above (Fig 5e, white arrow). This is also confirmed by the presence of oxygen rich regions inside each lamella (Fig 5e, white arrows). The remainder of the lamellar interior is a Ni-rich metallic matrix, forming an interconnected Ni-rich metallic core. At complete oxidation (Fig 5d) where complete conversion of Fe to Fe_3O_4 has been achieved, the lamellae and their secondary arms feature a cohesive, homogeneous oxide scale surrounding a tortuous metallic core which is crisscrossed by a network of oxide veins. At certain regions along the lamellae, the Ni-rich core appears to be completely transected by oxide-filled microchannels, and loses connectivity in-plane (though 3-D connectivity may remain), shown schematically in Fig 3c-e and by blue arrows in Fig 5f.

The Ni-rich core contains microscopic Kirkendall porosity (Fig 5f, black arrows), although significantly less so than in pure Fe foams [18], where the difference in diffusivities between Fe- and O- ions through the oxide layer leads to accumulation of Fe vacancies within the metallic core of the lamella. However, in the Fe-Ni system, the presence of the Ni may help prevent this imbalance. First, it is evident that Kirkendall porosity is not present after sintering, or upon the initial step of oxidation (Fig 5d). It has been previously hypothesized that these vacancies can initially be removed by dislocation climb in the FeO compound [20]. As oxidation proceeds however, this vacancy removal mechanism is limited by the total plastic deformation that can occur in the oxide layer. Because the Ni-rich core occupies a significant portion of the lamellar volume, the overall thickness of the scale layer and thus the concentration of vacancies forming on either side of the core are lower, partially explaining why there are fewer Kirkendall pores present than in pure-Fe after 1 cycle. Further, it is hypothesized that the Ni-rich metallic core can act as a vacancy sink, e.g. via dislocation climb or through diffusion at grain boundaries, thus preventing vacancy condensation into Kirkendall pores, consistent with previous literature [20].

3.2.3. Reduction

Reduction begins at the interface between the oxide scale and the Ni core (Fig. 3e), as described by Wilke and Dunand [20]. This is consistent with the catalytic effect of Ni in the reduction of Fe, visible in the significantly increased reduction rate in the Fe-25Ni foam, as compared to the Fe foam, observed during the *in-situ* x-ray diffraction experiments (Fig. 2); no visible oxide reduction initiates on the outer surfaces of the scales in contact with the reducing H_2 gas. Fig. 6 shows optical micrographs, SEM micrographs, and corresponding EDS maps for 10%, 45%, and 100% reduction of Fe.

The network of oxide veins within the lamellae has a strong effect during the surface-driven reduction reaction. The oxide veins are expected to contain small fractures (as well as channels formed from steam ingress and H_2 egress during the oxidation step) which now allow for H_2 ingress and rapid, early reduction. Combined with the large volumetric contraction from Fe_3O_4 to Fe, this leads to a rapid opening of most oxide veins (Supplementary Fig. 5, white arrows). Since these veins initially formed upon oxidation of an open submicron porosity network created during the lamella sintering, the resultant microchannel network produced on reduction is similarly open, providing ingress to hydrogen and egress for steam evolved during reduction. The expansion of the oxide likely widened the channels via plastic deformation of the surrounding metallic matrix.

As reduction proceeds, the metallic core grows outwards (Fig. 6b) concurrently with the outward diffusion of Ni into the newly reduced pure Fe regions, along with Fe diffusion inward to the originally Ni-rich core; the reduction of the oxide in the microchannels forms Fe-rich regions in the interior of the lamella (Fig 6d, green arrows). Along the expanding metallic core region, certain areas of wider oxide veins still exist, while other regions appear more fully dense (Fig 6c,d, white arrow). In these dense Fe-Ni regions, smaller Kirkendall pores can sinter by the fast diffusion of Fe, and the nearby availability of free surfaces (e.g. larger pores and microchannels).

As the metallic Fe-Ni core expands at the expenses of the outer Fe-oxide scales, adhesion is maintained between the two phases. This is unlike Fe foams, where lack of adhesion in the fully oxidized state (with no metallic core) leads to the lamella splitting longitudinally as the lamellae shrink during reduction. After reduction, these split lamellae, due to their larger width, are more prone to contact with their neighbors leading to sintering at contact points and overall foam densification ([18]). In the Fe-25Ni lamellae, lack of internal fracture may represent a better adhesion between oxide and metal, and higher strength of the metallic core (e.g., from solid-solution strengthening), and/or the effect of Ni diffusing towards the core-scale interface via bulk or even surface diffusion (via the micro-channels). The characteristic bulk diffusion distance predicted for Fe-25Ni is only 0.2 μm for 90 min at 800°C (with $D=6 \times 10^{-14}$ cm^2/s for Fe-25Ni), but the Ni core expands several micrometers in either direction (Fig 6b,c), indicating that a faster diffusion mechanism must be active [29].

Finally, the last part of the lamellae to reduce are the outside surfaces (Fig 6c). Due to the rapid reduction process, the amount of Ni that has fully diffused to the reaction front is somewhat limited at this point. This leaves a Fe-richer region on the outside of the lamellae, and as observed in Fe foams, the reduction to pure Fe, without local presence of Ni, causes fracture on the outside of the lamella (Fig 6c,f, blue arrows). This leaves fractured Fe-rich islands on the outside of the lamella, due to the lack of adhesion with the Ni-rich core, combined with the volumetric shrinkage associated with reduction. These cracks are small enough to close upon oxidization expansion in the beginning of the next cycle.

3.2.4. Rehomogenization

The entire reduction process occurs within the first 10 min of the reduction cycle (Supplementary Fig. 6). However, to avoid microstructural damage in the next cycle, the Ni must be rehomogenized into the lamellar volume, providing the mechanical strength that enables the lamella to resist fracture and returning each lamella to its initial state [20]. Thus, the remaining 80 min of the reduction half-cycle are used to homogenize the Ni concentration gradients (from core to surface) of the lamellae; the speed of this homogenization is affected by the microchannel network.

The effect of the microchannels on diffusion depends on their orientation with respect to the concentration gradient. Microchannels formed due to steam egress are oriented mostly parallel to the primary core-shell concentration gradient, as shown in Fig. 6b–f. These microchannels can provide short-circuit diffusion allow-

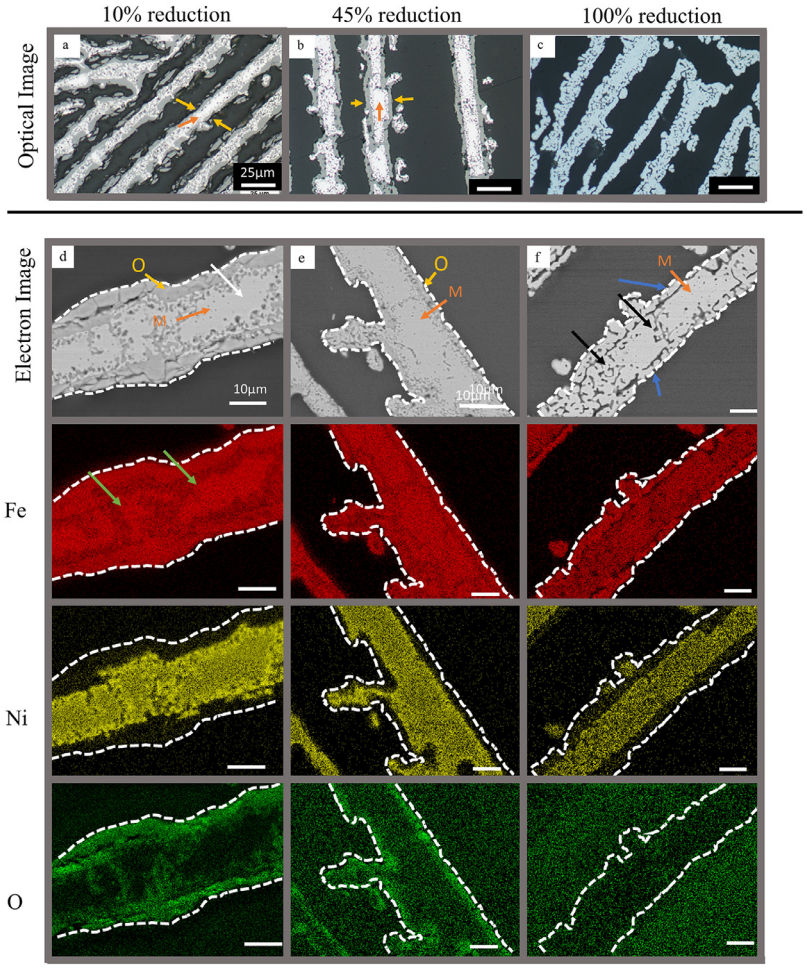

Fig. 6. Evolution of microstructure in Fe-25Ni lamellae during the first reduction half-cycle shown in radial cross sections with optical micrographs (a–c) and SEM micrographs with corresponding EDS maps (d–f) for 10% reduction (30 s), 45% reduction (2 min), and 100% reduction followed by rehomogenization (90 min). Yellow arrows indicate oxide scale (O) on lamellae. Orange arrows indicate metallic cores (M). White arrow shows example of dense region in the beginning of reduction. Blue arrows indicate regions where re-homogenization is not possible due to fracture. Black arrows signify regions where pores have coalesced after full chemical reduction of the foam. Dotted lines outline lamella surface to highlight differences in compositional makeup. Green arrows point to heavy scale regions formed along internal microchannels. Red arrows indicate delaminations.

ing for the rapid homogenization observed. Additional microchannels oriented orthogonally to the gradient are also observed, however. These are formed by decohesion of the thick oxide scale from the metallic core, as shown in Fig. 6f (red arrow). Delamination between these layers is particularly deleterious to the rehomogenization of the lamella, as Fe atoms are cut off from the metallic core and must diffuse in a tortuous route with little lateral driving force, resulting in incomplete rehomogenization in 90 min in regions near a scale delamination. During the subsequent cycle, however, these delamination events tend to diminish: a possible explanation is that during the next oxidation the delaminated region expands, contacting the main lamella and sintering, until the next reduction when it may or may not form again. Over multiple cycles this mechanism prevents delaminations from worsening.

While some of the gas-access channels might disappear via sintering or might pinch off into pores, most are too wide to fully close within 80 min. at 800 °C (Fig 6f, black arrows), unlike the much smaller, spherical Kirkendall pores. After 1 cycle, the average pore cross-sectional area within lamellae is ~9 μm^2 (~3 μm diameter), as compared to a submicron average pore diameter before cycling. In cross-sections, the area fraction of the gas-access channels is lower in the center of the lamellae, consistent with a high flux of Fe atoms during rehomogenization that may enhance sintering.

The microchannel network may be beneficial to the redox reaction by providing more surface area and easier gas access to lamellar volume; this effect competes, however, with densification and loss of gas access resulting in complex overall effects on successive cycles. Overall, the presence of Ni helps prevent the primary mechanism of fracture observed in Fe foams and provides a pathway to inhibiting and healing the continued formation of Kirkendall porosity, yielding a more cohesive lamellar structure after 1 redox cycle. The ability to recover the majority of the initial microstructure aids in the reversibility of this processes over multiple redox cycles.

3.3. Evolution of macrostructure and architecture

3.3.1. First cycle

Based on our understanding (described in the previous section) of the chemical and microstructural evolution of the Fe-25Ni foams during its first redox cycle, foams were subject to multiple consecutive redox cycles to assess long-term performance and degradation. Fig. 7 shows Fe-25Ni foams which were subjected to 1, 5 and 10 consecutive cycles. After the first cycle (Fig 7a), the morphology is similar to the initial as-cast structure, with well-separated, unfractured lamellae, but showing significant microchannel area within the lamellas. After 5 redox cycles (Fig 7b), the lamellar

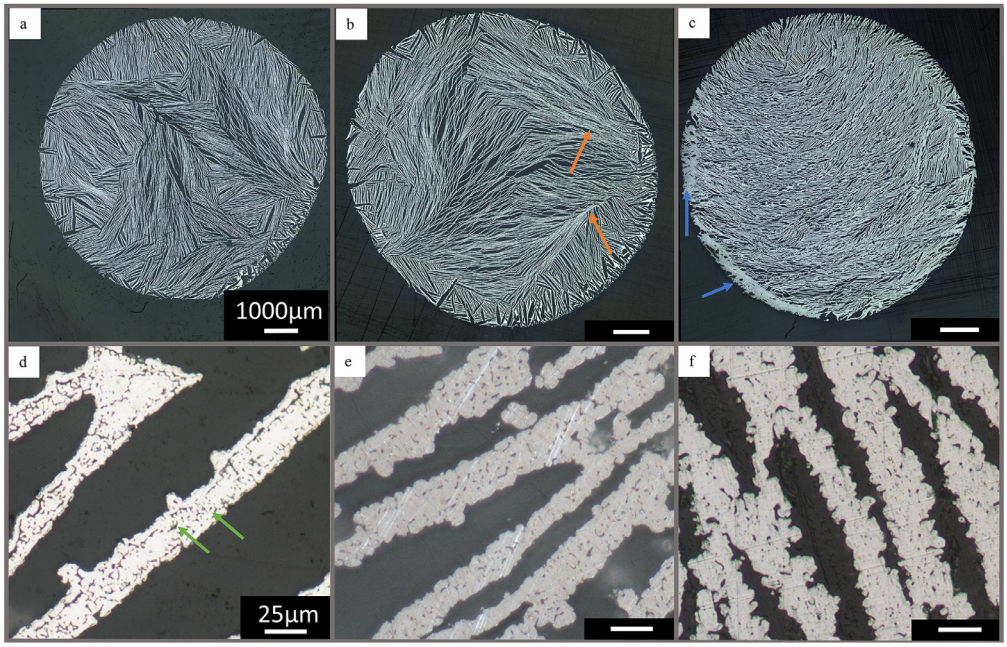

Fig. 7. Optical micrographs of full radial cross-sections of Fe-25Ni foams after various redox cycles; (a) 1 cycle, (b) 5 cycles, (c) 10 cycles; orange arrows highlight initial buckling-driven lamellae sintering, blue arrows show local outer shell formation due to lamellar tip sintering, (d–f) corresponding higher magnification optical micrographs of lamellae showing that they neither crack nor accumulate microporosity with increasing cycling, beyond that accumulated during the first cycle highlighted with green arrows.

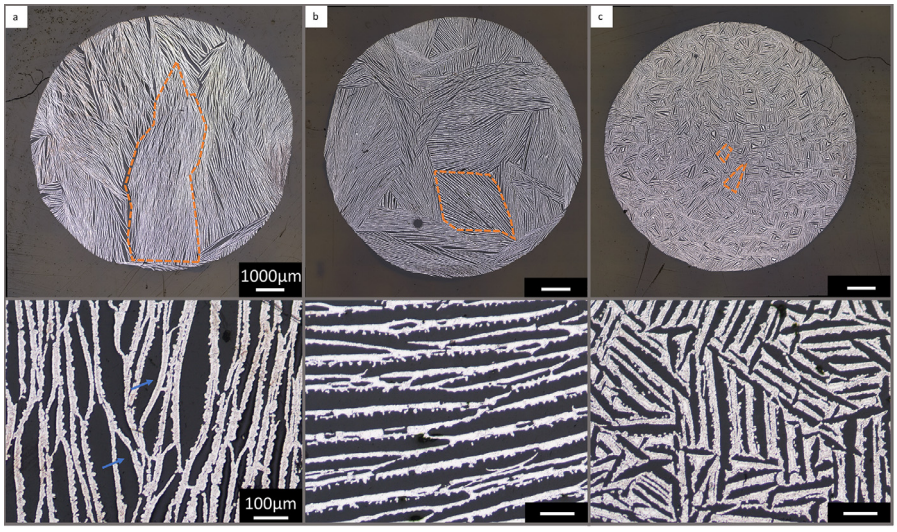

Fig. 8. Optical micrographs of full radial cross-sections of Fe-25Ni foams, after 1 redox cycle, with varying colony sizes: (a) sub-centimeter (0.5-1 cm), as used in the rest of this study, (b) millimeter (1-4 mm), (c) sub-millimeter (0.5-1 mm). Magnified micrographs are shown below each cross sections. Representative colonies are outlined in orange. Blue arrows highlight lamellae buckling in sub-centimeter colonies.

structure is maintained, and the microchannels and micropores created after each cycle (Fig. 7a) becomes less numerous, most probably via sintering and coalescence.

This stabilization of the porous microstructure reflects that these gas-access microchannels grow mostly during steam ingress in the first cycle, when their diameters are expanded from submicron- to micron-size via oxide formation. In successive cycles, the oxide that forms within the gas-access channels fills the existing space with little further increase, while sintering also takes place during rehomogenization, so that a steady-state channel diameter can be eventually expected. The measured microchannel area fraction within lamellae, as measured for the representative micrographs in Fig. 7d, e, and f, decreases from 8.0% after 1 cycle to 2.8% after 5 cycles and 2.5% after 10 cycles. The microchannels fill with oxide and empty during each redox cycle, and so healing becomes less and less effective, as the cycle number increases. The stability of these lamellar microchannels is key to preventing the degradation mechanisms present in pure Fe, where lamellae continuously accumulate porosity and cracks, by repeated expansion and fracture as cycles are accrued, reminiscent of ratchetting strain accumulated during freeze-thaw cycles [40].

A strategy to reduce lamellar buckling is to reduce the aspect ratio (width/thickness) of the lamellae by shrinking the colony sizes, as illustrated in Fig. 8(a–c) for three foams, with colony size decreasing from sub-centimeter (0.5–1 cm), to millimeter (1–4 mm), to sub-millimeter (0.5–1 mm), each having undergone 1

full redox cycle. All samples studied in the rest of this study and reported above possessed large colonies (0.5–1 cm). It is apparent that a smaller colony size helps to decrease the buckling effect that leads to long-term degradation in these foams, as shown in magnified micrographs in Fig. 8. Furthermore, various other changes in architecture of the freeze cast foams presented in literature - such as centrosymmetric alignment of lamellae radially, and cellular structures utilizing non-water based freeze casting methods - could help increase resistance to lamellar buckling during cycling of the foams [41–43].

3.3.2. Long-term cycling

As redox cycling continues past 5 cycles, buckling of the lamellae becomes more pronounced (Fig. 8, Supplementary Fig. 7). Buckling is a common feature of lamellae undergoing expansion, due to their high aspect ratio [44,45]. Specifically, in lamellar foams, the volumetric expansion of the oxide layer creates internal stresses within the lamellae as they are not free to expand at their ends, because of connections with neighboring lamellae dictated by colony orientation; the constrained expansion of the oxide layer leads to plastic buckling of the lamellae at 800 °C during oxidation. This is exacerbated by two primary factors: (i) a gradient of stresses due to uneven reaction rates across the entire foam, and (ii), pre-existing buckling of lamellae, created during reduction and sintering of the freeze-cast foams. This initial buckling, associated with the very large volumetric shrinkage during foam fabrication as explored previously [23], increases the contact points between neighboring lamellae and thus the extent of buckling during subsequent oxidation.

The presence of Ni helps to mitigate buckling by two mechanisms, strengthening and toughening: (i) the Ni-rich core benefits from solid solution strengthening compared to pure Fe, providing additional mechanical strength, and (ii) the Ni-rich core present throughout cycling (unlike the complete transformation to oxide in the Fe-foams) helps mitigate fracture during buckling by providing a ductile skeleton within the lamellar structure. These mechanisms maintain most of the rigid lamellar structure after 10 cycles (Fig 7c), though some buckling still occurs locally.

Fig. 9 shows changes in volume, channel porosity, lamellar thickness, and channel thickness for Fe and Fe-25Ni foams over the first 10 redox cycles. As shown in Fig 9a, the Fe-Ni foams exhibit a much smaller volumetric shrinkage as compared to Fe foams; this shrinkage is driven by the buckling and subsequent sintering of lamellae. An alternative shrinkage mechanism - the high temperature densification of individual lamellae – is found to be negligible by an additional experiment: an Fe-25Ni foam maintained in an inert Ar environment at 800°C for the same duration as the total rehomogenization period for 20 cycles (1600 min) showed no volumetric shrinkage. This demonstrates that the volumetric shrinkage observed in cycled foams reflects only degradation mechanisms produced by the redox cycling itself.

Fig. 9b shows that channel porosity in Fe-25Ni foams (as measured on full cross-sections such as those shown in Fig. 6 and 7) is 66–72% before cycling, in a similar range as that of Fe foams; sample-to-sample variations are expected to be primarily due to differences in colony orientation, leading to differing shrinkages during reduction and sintering from the freeze-cast state [23]. Over 10 cycles, the Fe-25Ni foams maintains ~40% channel porosity, a value sufficient for gas flow to completely oxidize and reduce the lamellae in the given cycle periods. By contrast, Fe foam channel porosity decreases more rapidly, to 21% after 5 cycles. This value is nearly unchanged after 10 cycles, with the ~20% channel porosity consisting of large chambers (Supplementary Fig. 8, blue arrows), hundreds of micrometers wide, which are trapped between buckled lamellae and have a much-reduced accessibility to gas, rather than open, parallel channels allowing full gas access.

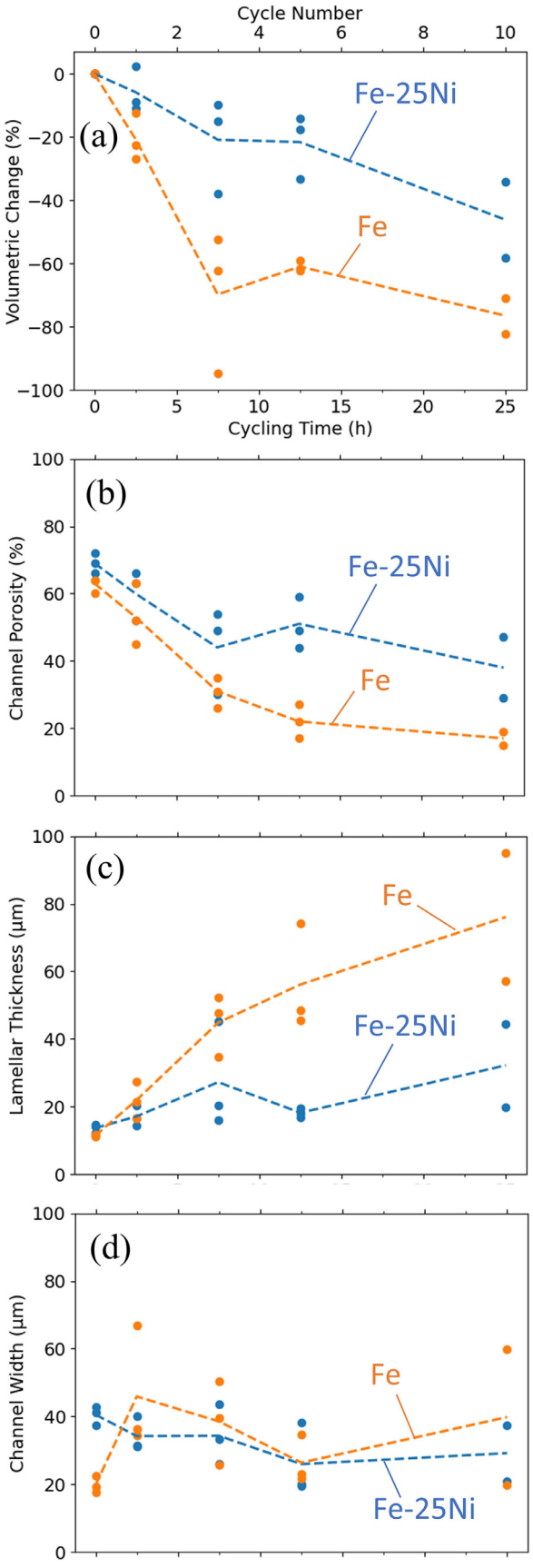

Fig. 9. Evolution with cycling time (cycle number) in Fe-Ni and Fe foams of (a) volumetric shrinkage, (b) foam channel porosity, (c) lamellar thickness and (d) channel width. Lines connect average values: each data point is an individual sample.

As shown in Fig. 9c, the Fe-25Ni lamellar thickness remains similar to the initial average lamellar thickness throughout the first 5 cycles; this is unlike the lamellar swelling observed in Fe foams resulting from lamellae splitting due to accumulation of pores and cracking at the interface, which also causes lamellae to merge via sintering to their neighbors, thus strongly increasing the average thickness. The near constant Fe-25Ni lamellar thickness is achieved via Fe and Ni re-homogenization within lamellae after each reduction, as discussed above. The modest increase in average Fe-25Ni wall thickness after 10 cycles is due to densified regions along the outside of the foam (Fig. 7c, blue arrows). The foam surface is particularly unstable, as it consists entirely of lamellar tips, which have high curvature and are mechanically unsupported; this leads to lamellar tips flaring and then sintering with each other, exacerbating densification at the boundary of the foam, as discussed in Ref. [18] for Fe foams which exhibit the formation of a dense shell around the entirety of the foam after 5 cycles, rather than in a few surface regions in Fe-25Ni foams after 10 cycles (Fig. 7c, blue arrows).

Finally, as shown in Fig. 9(d), interlamellar channel width in Fe-25Ni foams decreases slightly with the first 3 cycles, reflecting the overall shrinkage of the foam driven by lamellar buckling, but this levels out with further cycling. In contrast, Fe foams show an increase in channel width initially. This is because of buckling lamellae that sinter together, thus closing many channels entirely and leaving fewer, larger channels (turning into the chambers described above). The channel width then decreases in Fe foams, as remaining individual lamellae continue to deform and contact the dense, sintered regions. As shown in Figs. 9(c,d), the near-constant channel width and wall thickness measured in Fe-25Ni foams are consistent with a much improved resistance against lamellar deformation (by buckling of splitting) and sintering, as compared to the Fe-foam.

4. Conclusions

The degradation of lamellar Fe foams during hydrogen/steam redox cycling (relevant to Fe-air battery systems), originates from the large volumetric expansion/shrinkage combined with diffusional flux imbalance, which leads to lamellar buckling, microporosity formation, internal fracture, and sintering, despite a lamellar architecture with wide channels designed to allow for volumetric changes. We show here that these damage mechanisms, which choke gas exchange, can be mitigated by alloying with 25 at.% Ni, thus enabling Fe-25Ni foams to better survive multiple redox cycles.

This improvements in cycling resistance provided by nickel alloying can be explained by three main mechanisms:

(i) On foam oxidation, Ni is rejected to the core of the lamellae, forming a metallic Ni-rich core that mitigates the formation of Kirkendall porosity and helps limit lamellar buckling driven by internal oxidation stresses as compared to pure Fe. This occurs via solid solution strengthening and toughening, by providing adhesion to the oxide scale, and by preventing lamellar splitting.

(ii) On foam oxidation, micro-channels formed within each lamella during the initial sintering of the foam enable internal, volumetric oxidation forming interconnected oxide network which, after oxide reduction, becomes an open microchannel network. This network is responsible for rapid surface diffusion enabling rehomogenization, but misoriented microchannels can interrupt diffusional pathways from shell to the core of each lamella.

(iii) During foam reduction, the Ni core provides a reaction site for the reduction of iron oxide, both at the outer scale and the inner microchannels. Nickel also prevents delamination of the scale from the metallic core by rapidly inter-diffusing with newly reduced Fe. At the end of the cycle, the reduced Fe-rich shell and Ni-rich core have fully inter-diffused, restoring the initial homogenous composition of the Fe-25Ni lamellae.

Nickel additions also alter reaction kinetics. *In-situ* XRD shows that, compared to pure Fe foams, Fe-Ni foams have slightly slower oxidation rate by slowing the diffusion of Fe to the oxidizing surface. Reduction, however, is catalyzed by the presence of Ni, significantly increasing reaction rate. Observation of the rapid change in composition of the Fe-Ni core upon reduction confirms the fast interdiffusion of Fe and Ni, allowing for the rehomogenization of the lamellae to a uniform Fe-25Ni composition, which enables further cycling.

Over multiple cycles (up to 10), the Fe-Ni foams maintain a higher macro-channel volume than Fe foams, and lamellar microporosity achieved after the first cycle remains constant, allowing for sufficient gas flow throughout cycling. By reducing lamellar colony sizes during the freeze-casting fabrication step of the foams, buckling of lamellae can further be mitigated by decreasing their aspect ratio, further increasing the lifetime and usability of Fe-25Ni foams.

Disclosure

DCD discloses a financial interest in Cell Mobility, Inc., a company involved with metal foams.

Declaration of Competing Interest

The authors declare that they have no known competing financial interests or personal relationships that could have appeared to influence the work reported in this paper.

Acknowledgments

The research was funded by the US National Science Foundation under grant CMMI-2015641. The authors acknowledge Dr. Christos Malliakas (NU) for assistance with XRD experiments, Dr. Christoph Kenel (NU) for help with XRD analysis, and Dr. Stephen Wilke (Materials Development Inc.) for insightful discussions. Experiments and characterization made use of the Materials Characterization and Imaging Facility, the NUANCE Center (supported by SHyNE under NSF ECCS-1542205, MRSEC under NSF DMR-1720139, the International Institute for Nanotechnology, the Keck Foundation, and the State of Illinois), and the IMSERC X-Ray facility (supported by SHyNE under NSF ECCS-2025633) at Northwestern University (NU).

Supplementary materials

Supplementary material associated with this article can be found, in the online version, at doi:10.1016/j.actamat.2022.118148.

References

[1] C. Wang, et al., Recent progress of metal–air batteries—a mini review, Appl. Sci. 9 (2019) 2787.
[2] N. Chawla, Recent advances in air-battery chemistries, Mater. Today Chem. 12 (2019) 324–331.
[3] X. Zhao, Y. Gong, X. Li, N. Xu, K. Huang, Cyclic durability of a solid oxide Fe-air redox battery operated at 650°C, J. Electrochem. Soc. 160 (2013) A1716–A1719.
[4] A. Dinesh, et al., Iron-based flow batteries to store renewable energies, Environ. Chem. Lett. 16 (2018) 683–694.
[5] W. Drenckhahn, et al., A novel high temperature metal-air battery, Electrochem. Soc. 50 (2013) 125–135.
[6] R. Mckerracher, C. Ponce De León, R.G.A. Wills, F.C. Walsh, A review of the iron-air secondary battery for energy storage, Chempluschem 80 (2014) 323–335.
[7] S. Trocino, M. Lo Faro, S.C. Zignani, V. Antonucci, A.S. Aricò, High performance solid-state iron-air rechargeable ceramic battery operating at intermediate temperatures (500–650 °C), Appl. Energy 233–234 (2019) 386–394.

[8] C. Zhang, K. Huang, An intermediate-temperature solid oxide iron–air redox battery operated on O_2—chemistry and loaded with Pd-catalyzed iron-based energy storage material, ACS Energy Lett. 1 (2016) 1206–1211.
[9] H. Ohmori, H. Iwai, Simulation of solid oxide iron-air battery: effects of heat and mass transfer on charge/discharge characteristics, J. Power Sources 286 (2015) 264–275.
[10] X. Zhao, X. Li, Y. Gong, K. Huang, Enhanced reversibility and durability of a solid oxide Fe–air redox battery by carbothermic reaction derived energy storage materials, Chem. Commun. 50 (2013) 623–625.
[11] Y. Saito, F. Kosaka, N. Kikuchi, H. Hatano, J. Otomo, Evaluation of microstructural changes and performance degradation in iron-based oxygen carriers during redox cycling for chemical looping systems with image analysis, Ind. Eng. Chem. Res. 57 (2018) 5529–5538.
[12] C.M. Berger, et al., Development of storage materials for high-temperature rechargeable oxide batteries, J. Energy Storage 1 (2015) 54–64.
[13] M. Ebner, F. Marone, M. Stampanoni, V. Wood, Visualization and quantification of electrochemical and mechanical degradation in li ion batteries, Science 342 (2013) 716–720 (80-.).
[14] O.O. Taiwo, et al., Investigation of cycling-induced microstructural degradation in silicon-based electrodes in lithium-ion batteries using X-ray nanotomography, Electrochim. Acta 253 (2017) 85–92.
[15] S. Moser, C. Kenel, L.A. Wehner, R. Spolenak, D.C. Dunand, 3D ink-printed, sintered porous silicon scaffolds for battery applications, J. Power Sources 507 (2021) 230298.
[16] S.K. Wilke, D.C Dunand, Structural evolution of directionally freeze-cast iron foams during oxidation/reduction cycles, Acta Mater. 162 (2019) 90–102.
[17] S.K. Wilke, D.C Dunand, Finite element model for coupled diffusion and elastoplastic deformation during high-temperature oxidation of Fe to FeO, J. Electrochem. Soc. 167 (2020) 080532.
[18] S.K. Wilke, D.C. Dunand, In operando tomography reveals degradation mechanisms in lamellar iron foams during redox cycling at 800°C, J. Power Sources 448 (2020) 227463.
[19] J. Eigen, B. Rutjens, M. Schroeder, Partial redox cycling of composite storage materials for rechargeable oxide batteries, J. Energy Storage 43 (2021) 103161.
[20] S.K. Wilke, D.C Dunand, Fe-Ni foams self-heal during redox cycling: via reversible formation/homogenization of a ductile Ni scaffold, J. Mater. Chem. A 8 (2020) 19375–19386.
[21] C. Stolze, T. Janoschka, U.S. Schubert, F.A. Müller, S. Flauder, Directional solidification with constant ice front velocity in the ice-templating process, Adv. Eng. Mater. 18 (2016) 111–120.
[22] R. Dougherty, K.H. Kunzelmann, Computing local thickness of 3D structures with imageJ, Microsc. Microanal 13 (2007) 1678–1679.
[23] S.K. Wilke, J.B. Mack, C. Kenel, D.C. Dunand, Evolution of directionally freeze–cast Fe_2O_3 and Fe_2O_3+NiO green bodies during reduction and sintering to create lamellar Fe and Fe-20Ni foams, J. Alloys Compd. 889 (2022) 161707.
[24] K.M. Thyng, C.A. Greene, R.D. Hetland, H.M. Zimmerle, S.F. DiMarco, True colors of oceanography, Oceanography 29 (2016) 9–13.
[25] S. He, et al., Baseline correction for Raman spectra using an improved asymmetric least squares method, Anal. Methods 6 (2014) 4402–4407.
[26] M. Newville, T. Stensitzki, Non-linear least-squares minimization and curve-fitting for python, Non-Linear Least-Squares Minimization and Curve-Fitting for Python 65 (2018).
[27] O. Kubaschewski, Iron - Binary phase diagrams. Materials Engineering 2, Springer-Verlag Heidelberg GmbH, 1982.
[28] A. Thursfield, A. Murugan, R. Franca, I.S Metcalfe, Chemical looping and oxygen permeable ceramic membranes for hydrogen production – a review, Energy Environ. Sci. 5 (2012) 7421–7459.
[29] E.A. Brandes, G.B. Brook, Smithells Metals Reference Book, Butterworth Heinemann, 1992.
[30] M. Wang, N. Li, Z. Wang, C. Chen, Z. Zhan, Electrochemical performance and redox stability of solid oxide fuel cells supported on dual-layered anodes of Ni-YSZ cermet and Ni–Fe alloy, Int. J. Hydrog. Energy 47 (2022) 5453–5461.
[31] X. Yuan, T. Pu, M. Gu, M. Zhu, J. Xu, Strong metal—support interactions between nickel and iron oxide during CO_2 hydrogenation, ACS Catal. 11 (2021) 11966–11972.
[32] K.M. Jeerage, S.L. Candelaria, S.M. Stavis, Rapid synthesis and correlative measurements of electrocatalytic nickel/iron oxide nanoparticles, Sci. Rep. 8 (2018).
[33] A.R. Puigdollers, P. Schlexer, S. Tosoni, G. Pacchioni, Increasing oxide reducibility: the role of metal/oxide interfaces in the formation of oxygen vacancies, ACS Catal. 7 (2017) 6493–6513.
[34] X. Zhao, Y. Gong, X. Li, N. Xu, K. Huang, Performance of solid oxide iron-air battery operated at 550°C, J. Electrochem. Soc. 160 (2013) A1241–A1247.
[35] H. Riedel, J. Svoboda, A theoretical study of grain growth in porous solids during sintering, Acta Metall. Mater. 41 (1993) 1929–1936.
[36] Y. Liu, B.R. Patterson, Grain growth inhibition by porosity, Acta Met. Mater. 41 (1993) 2651–2656.
[37] C. Wagner, Internal oxidation of Cu-Pd and Cu-Pt alloys, Corros. Sci. 8 (1968) 889–893.
[38] A. Combe, J. Cabane, Mechanism of internal oxidation in silver alloys, Oxid. Met. 21 (1984) 21–37 1984 211.
[39] S. Guruswamy, S.M. Park, J.P. Hirth, R.A. Rapp, Internal oxidation of Ag-in alloys: stress relief and the influence of imposed strain, Oxid. Met. 26 (1986) 77–100 1986 261.
[40] B. Lin, F. Zhang, D. Feng, K. Tang, X. Feng, Accumulative plastic strain of thawed saturated clay under long-term cyclic loading, Eng. Geol. 231 (2017) 230–237.
[41] Y. Tang, Q. Miao, S. Qiu, K. Zhao, L. Hu, Novel freeze-casting fabrication of aligned lamellar porous alumina with a centrosymmetric structure, J. Eur. Ceram. Soc. 34 (2014) 4077–4082.
[42] S. Deville, Freeze-casting of porous ceramics: a review of current achievements and issues, Adv. Eng. Mater. 10 (2008) 155–169.
[43] P.J. Lloreda-Jurado, et al., Structure-processing relationships of freeze-cast iron foams fabricated with various solidification rates and post-casting heat treatment, J. Mater. Res. (2020), doi:10.1557/jmr.2020.175.
[44] A. Ojuva, et al., Mechanical performance and CO_2 uptake of ion-exchanged zeolite a structured by freeze-casting, J. Eur. Ceram. Soc. 35 (2015) 2607–2618.
[45] H. Bai, Y. Chen, B. Delattre, A.P. Tomsia, R.O Ritchie, Bioinspired large-scale aligned porous materials assembled with dual temperature gradients, Sci. Adv. 1 (2015).